Heat-Exchange Pressure Swing Adsorption Process for Hydrogen Separation

Jang-Jae Lee, Min-Kyu Kim, and Dong-Geun Lee
Dept. of Chemical and Biomolecular Engineering, Yonsei University, Seodaemun-Gu, Seoul 120-749, Korea

Hyungwoong Ahn
Refining Process Technologies, SK Energy Institute of Technology, Yuseong-Gu, Daejeon 305-702, Korea

Myung-Jun Kim
CRD Center, SK Energy Institute of Technology, Yuseong-Gu, Daejeon 305-702, Korea

Chang-Ha Lee
Dept. of Chemical and Biomolecular Engineering, Yonsei University, Seodaemun-Gu, Seoul 120-749, Korea

DOI 10.1002/aic.11544
Published online June 10, 2008 in Wiley InterScience (www.interscience.wiley.com).

A current focus in the energy field is on the use of hydrogen in fuel cells. Development of a hydrogen station system is important to the commercialization of fuel cells and fuel cell powered vehicles. In this study, the heat-exchange pressure swing adsorption (HE-PSA) was developed to design a compact H_2 PSA process for small spatial occupancy in the hydrogen station. The adsorption dynamics and performance of the newly designed bed were compared with those of a conventional bed by using a quaternary mixture (H_2/CO_2/CH_4/CO 69:26:3:2 vol %) which is generally obtained from the steam-reforming reaction of natural gas. Because the detrimental exothermic/endothermic heat effects accompanied by the adsorption/desorption steps were reduced by heat exchange between the adsorption beds, the separation performance of the HE-PSA was higher than that of a conventional PSA. In addition, the spatial occupancy of the beds could be significantly reduced, compared with a conventional PSA, because the single annular-type bed performed the function of two beds in the HE-PSA. © 2008 American Institute of Chemical Engineers *AIChE J,* 54: 2054–2064, 2008
Keywords: heat-exchange, PSA, hydrogen station, hydrogen separation

Introduction

Today our industry's heavy reliance on fossil fuels is a central obstacle to improving air quality and preventing catastrophic climate change. Hydrogen energy is considered one of the most important renewable energy sources for the future, not only as a raw material for the chemical and petroleum industries, but also in the fuel cell.[1,2]

Development of the hydrogen station system is a crucial technology for the commercialization of fuel cells and fuel cell powered vehicles. Generally, the hydrogen station consists of an on-site hydrogen production process that includes a desulfurizer, reformer, water gas shift (WGS) reactor, and an H_2 separation apparatus. The typical on-site posttreatment process includes a compressor, storage unit, and distributor.

Correspondence concerning this article should be addressed to C.-H. Lee at leech@yonsei.ac.kr.

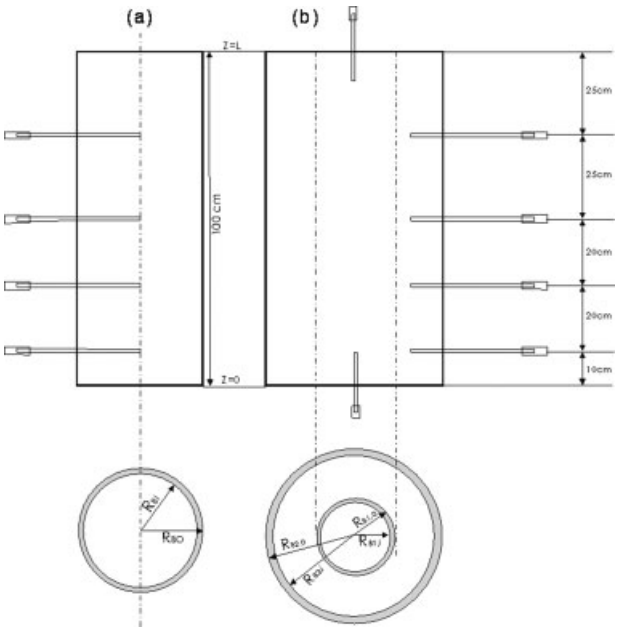

Figure 1. Schematic diagram and spatial coordinate of (a) the conventional adsorption bed and (b) the compact heat-exchange beds.

In the conventional steam methane reforming (SMR) process for a hydrogen station, the effluent from the WGS reactor is further cooled and then fed to a multicolumn pressure swing adsorption (PSA) process at a pressure of 345–4137 kPa.[3,4] A multicolumn PSA process containing two to four adsorption beds is generally used in conjunction with a combination of various PSA process steps. The net hydrogen recovery from the PSA process and its adsorbent inventory depend on many variables. In particular, the CO and CO_2 concentrations of the feed gas are critical in determining the design and efficiency of separation of the PSA process because bulk CO_2 is difficult to desorb and dilute CO is difficult to adsorb.[4–6]

For a hydrogen station, such as a small to medium-sized hydrogen plant, to be space efficient and allow for quick installation, it is typically built in a modular configuration. The conventional PSA system occupies a lot of space in the hydrogen station and adsorption beds require the most space in the PSA process. Therefore, it is important to design a compact PSA process by modifying the fixed-bed geometry in the symmetric multibed system.

The purpose of this study is to develop the compact PSA process for high-purity H_2 generation in the on-site H_2 station process. To reduce both the space occupied by the adsorption beds and the detrimental heat effects from the process, the annular-type bed (a dual bed: one bed placed inside another bed) was designed. The adsorption dynamics of the newly designed bed were compared with those of a conventional (single) bed by using the quaternary mixture ($H_2/CO_2/CH_4/CO$ 69:26:3:2 vol %) which is generally obtained from the steam reforming reaction of natural gas. The separation performance of a two-bed HE-PSA using one dual bed was compared with that of a conventional PSA using two single beds.

Experiment

The schematic and characteristics of conventional single bed and heat-exchange dual bed are shown in Figure 1 and Table 1, respectively.

The conventional adsorption bed is 100 cm long and 3.5 cm I.D., made of stainless steel with a wall thickness of 2.67 mm. Four resistance temperature detectors (RTD Pt 100Ω) were installed at the positions of 10, 30, 50, and 75 cm from the feed end to probe the temperature variation inside the bed.

Meanwhile, the heat-exchange dual bed was constructed as a standard shell and tube type. The inner (3.15 cm I.D.) and outer beds (4.75 cm I.D) with 100 cm length were made of brass and stainless steel, respectively. The bed volumes

Table 1. Characteristics of Adsorption Bed and Adsorbent

		Heat-Exchange Dual Bed	
Adsorption Bed	Conventional Bed	Inner Bed	Outer Bed
Length	100 cm	100 cm	100 cm
Inside diameter	3.5 cm	3.16 cm	4.75 cm
Outside diameter	4.04 cm	3.54 cm	6.8 cm
Materials of bed	Stainless steel	Brass	Stainless steel
Heat capacity of wall	0.502 J/g K	0.377 J/g K	0.502 J/g K
Density of wall	7.83 g/cm^3	8.47 g/cm^3	7.83 g/cm^3
Heat transfer coefficient: h_i		0.368×10^{-2} J/cm^2 s K	3.684×10^{-2} J/cm^2 s K
h_o		0.571×10^{-2} J/cm^2 s K	0.143×10^{-2} J/cm^2 s K
K_L		1.0×10^{-5} J/m s K	
D_L		1.0×10^{-5} cm^2/s	
$C_{p,g}$		9.24×10^{-1} J/g K	
μ		2.0×10^{-5} Pa s	
Adsorbents		Activated carbon	
Type		Granular	
Normal pellet size		10–12 mesh	
Average pellet size		0.115 cm	
Pellet density		0.85 g/cm^3	
Bulk density		0.482 g/cm^3	
External void fraction		0.433	
Heat capacity		1.046 J/g K	

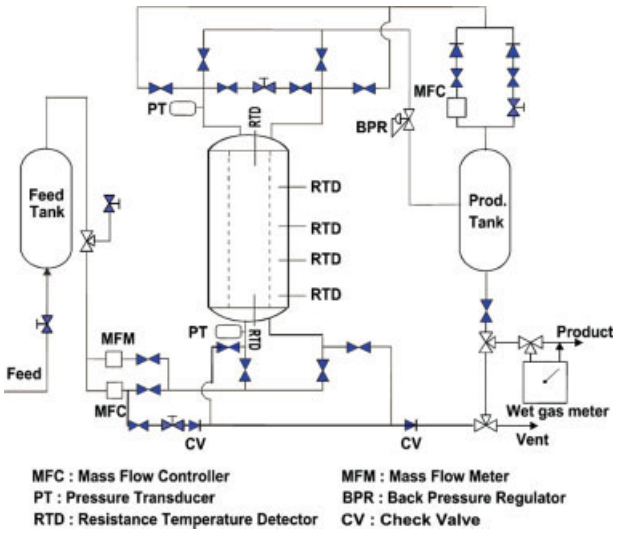

Figure 2. Schematic of a two-bed PSA system.

[Color figure can be viewed in the online issue, which is available at www.interscience.wiley.com.]

of the inner and outer beds were identical, but the volume of each bed in the dual bed was 81% of that of the conventional single bed. Four RTDs were installed at the outer bed at the same positions used for the single bed. In addition, two RTDs were arranged along the inner bed at the positions of 10 and 90 cm from the feed end.

The schematic of the experimental apparatus is shown in Figure 2. Two pressure transducers were located at the feed and product ends to measure the pressure variation. The precalibrated mass flow controller (Bronkhorst High-tech, F-201C, The Netherlands) was installed between the feed tank and the adsorption bed to control the feed flow rate. The total amount of gas was confirmed by a wet gas meter (Shinagawa, W-NK-1B, Japan). The electrical back-pressure regulator (Bronkhorst High-tech, P-702C, The Netherlands) between the adsorption bed and the product tank was installed to maintain constant adsorption pressure in the bed. Effluent stream was sampled between the back-pressure regulator and the product tank and was analyzed using a mass spectrometer (Balzers, QME 200, Germany). All the data, including concentration, temperature, pressure, and flow rate, were saved on a computer. Details of the equipment and the operating procedures used are described in the previous work.[7]

The hydrogen quaternary mixture ($H_2/CO_2/CH_4/CO$; 69/26/3/2 vol %), which is a main composition in the steam methane reforming of natural gas, was used as feed gas, and activated carbon (Calgon Carbon Co, PCB) was applied as an adsorbent to breakthrough and PSA experiments. Before the experimental runs, the adsorbent was regenerated at 423 K for 8 h. The breakthrough experiments were conducted at the bed saturated by pure H_2 (99.99+%).

To compare the PSA performance using a dual bed with that using single bed, the following six-step two-bed PSA process was applied to the quaternary H_2 mixture: (1) pressurization with the feed gas (PR), (2) high-pressure adsorption (AD), (3) depressurizing pressure equalization (DPE), (4) blow down (BD), (5) purge with a light product (PG), and (6) pressurizing pressure equalization (PPE).[8,9] The cyclic sequence and a simple flow diagram are illustrated in Figure 3. The specific experimental operating conditions, such as adsorption step time, feed flow rate, purge rate, and adsorption pressure, are listed in Table 2.

Mathematical Model

To understand the dynamic behavior of each adsorption bed, a set of mathematical models was developed. A complete nonisothermal dynamic model was considered in this study with the following assumptions[10–13]: (i) the gas phase behaves as an ideal gas mixture, (ii) radial concentration and temperature gradients are negligible, (iii) thermal equilibrium between adsorbents and bulk flow is assumed, (iv) the flow pattern is described by the axially dispersed plug flow model, (v) axial conduction in the wall can be neglected, and (vi) the pressure drop along the bed is considered using Ergun's equation.[14–17]

Using the flow pattern described by axial dispersion plug flow and the above assumptions, the material balances of each component for the bulk phase in the adsorption column are given by

$$-D_L\frac{\partial^2 C_i}{\partial z^2}+\frac{\partial(uC_i)}{\partial z}+\frac{\partial C_i}{\partial t}+\rho_p\left(\frac{1-\varepsilon}{\varepsilon}\right)\frac{\partial \overline{q_i}}{\partial t}=0 \quad (1)$$

Overall mass balance also can be written as

$$\frac{\partial(uC)}{\partial z}+\frac{\partial C}{\partial t}+\rho_p\left(\frac{1-\varepsilon}{\varepsilon}\right)\sum_{i=1}^{n}\frac{\partial \overline{q_i}}{\partial t}=0 \quad (2)$$

Assuming thermal equilibrium between fluid and particles, the energy balance for the gas and solid phases is given by

$$-K_L\frac{\partial^2 T}{\partial z^2}+\varepsilon\rho_g C_{pg}\frac{\partial(uT)}{\partial z}+\left(\varepsilon_t\rho_g C_{pg}+\rho_B C_{ps}\right)\frac{\partial T}{\partial t}-\rho_B\sum_{i=1}^{n}\left(-\Delta\overline{H_i}\right)\frac{\partial \overline{q_i}}{\partial t}+\frac{2h_i}{R_{Bi}}(T-T_w)=0 \quad (3)$$

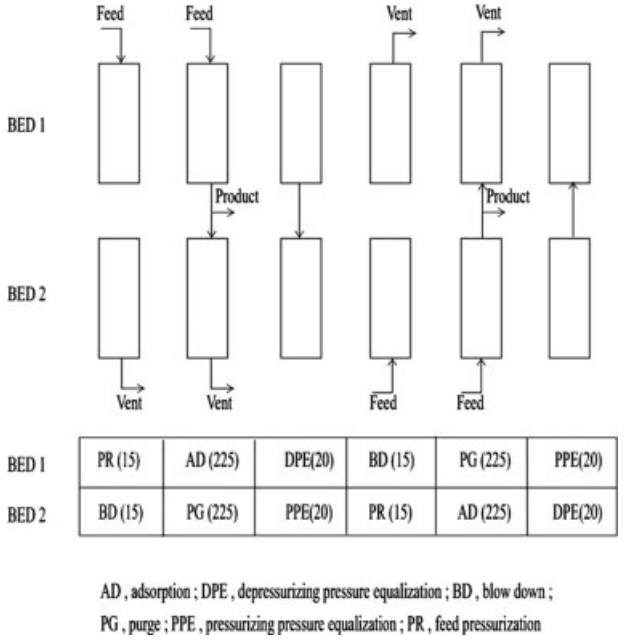

Figure 3. Flow diagram and cycle sequence of a six-step PSA process.

Table 2. Experimental Conditions of Breakthrough and PSA Runs

Breakthrough Conditions					
Run No.	Bed Type	Bed Initial Condition	Feed Flow Rate [LPM]	Adsorption Pressure [kPa]	Purge Rate [LPM]
Run 1	Conventional	H_2 saturated	7	912	–
Run 2	Inner	H_2 saturated	7	912	–
	Outer	H_2 saturated	7	912	–
Run 3	Inner	H_2 saturated	7	912	–
	Outer	H_2 saturated	7	912	–
Run 4	Inner	H_2 saturated	7	912	–
	Outer	H_2 mixture	–	152	3.5
Run 5	Inner	H_2 mixture	–	152	3.5
	Outer	H_2 saturated	7	912	–

HE-PSA conditions				
	Adsorption Pressure [kPa]	Feed Flow Rate [LPM]	Purge Rate [LPM]	Adsorption Step Time [s]
Run 6	912	7	0	225
Run 7	912	7	0.5	225
Run 8	912	7	1	225
Run 9	912	7	1.5	225
Run 10	912	7	0.5	200
Run 11	912	7	0.5	250
Run 12	912	7	0.5	275

where ε_t is the total void fraction ($=\varepsilon + (1 - \varepsilon)\alpha$), ρ_B is the bed density, ($=(1 - \varepsilon)\rho_p$) and K_L is the effective axial thermal conductivity used to take into account effective conduction in the axial direction.[6,18]

In large commercial units, the last term in energy balance could be neglected because heat transfer to the wall is not significant in comparison with the amount of heat of adsorption, if the length-to-diameter ratio is minimal. However, since the diameter of the single bed used in the present study was rather small, heat loss through the wall and heat accumulation in the wall could not be ignored. Therefore, another energy balance for the wall of the adsorption bed was introduced with the intention of disregarding axial conduction in the wall:

$$\rho_w C_{pw} A_w \frac{\partial T_w}{\partial t} = 2\pi R_{Bi} h_i (T - T_w) - 2\pi R_{Bo} h_o (T_w - T_{atm}) \quad (4)$$

where $A_w = \pi(R_{Bo}^2 - R_{Bi}^2)$.

To design a compact PSA process as well as reduce the detrimental exothermic/endothermic heat effects accompanied by the adsorption/desorption steps, the standard shell-and-tube type dual bed was used.

As shown in Figure 1b, a single tube, as an inner bed, is located inside the other bed. Therefore, the heat exchange between the inner and outer beds occurs through the brass wall. On the other hand, the heat exchange in the outer bed occurs in two parts: heat exchange between the inner and outer beds and between the outer bed and its surroundings. The annular-design bed is similar to a double-pipe heat exchanger in which the shell and tube are equal in volume. The energy balances in the inner and outer beds, with heat transferred to the adjacent column walls, were constructed as follows:

Energy balance in the inner bed:

$$-K_L \frac{\partial^2 T_1}{\partial z^2} + \varepsilon \rho_g C_{pg} \frac{\partial (u_1 T_1)}{\partial z} + \left(\varepsilon_t \rho_g C_{pg} + \rho_B C_{ps}\right) \frac{\partial T_1}{\partial t} - \rho_B \sum_{i=1}^{n} \left(-\Delta \overline{H_i}\right) \frac{\partial \overline{q_i}}{\partial t} + \frac{2h_{1,i}}{R_{B1,i}} (T_1 - T_{w1}) = 0 \quad (5)$$

Energy balance in the outer bed:

$$-K_L \frac{\partial^2 T_2}{\partial z^2} + \varepsilon \rho_g C_{pg} \frac{\partial (u_2 T_2)}{\partial z} + \left(\varepsilon_t \rho_g C_{pg} + \rho_B C_{ps}\right) \frac{\partial T_2}{\partial t} - \rho_B \sum_{i=1}^{n} \left(-\Delta \overline{H_i}\right) \frac{\partial \overline{q_i}}{\partial t} + \frac{2\eta h_{1,o}}{R_{B1,o}} (T_2 - T_{w1}) + \frac{2h_{2,i}}{R_{B2,i}} (T_2 - T_{w2}) = 0 \quad (6)$$

where subscripts 1 and 2 refer to bed 1 (inner bed) and 2 (outer bed), respectively, and η is the fin efficiency. In this study, however, extended heat-transfer surfaces were not used (i.e., $\eta = 1$) so that the parameter was only applied for the theoretical runs.

The energy balance equations of the wall, like Eq. 4, were also applied to the two bed walls, inner tube and outer shell.

$$\rho_{w1} C_{pw1} A_{w1} \frac{\partial T_{w1}}{\partial t} = 2\pi R_{B1,i} h_{1,i} (T_1 - T_{w1}) - 2\pi R_{B1,o} h_{1,o} (T_{w1} - T_2) \quad (7)$$

$$\rho_{w2} C_{pw2} A_{w2} \frac{\partial T_{w2}}{\partial t} = 2\pi R_{B2,i} h_{2,i} (T_2 - T_{w2}) - 2\pi R_{B2,o} h_{2,o} (T_{w2} - T_{atm}) \quad (8)$$

where $A_{w1} = \pi(R_{B1,o}^2 - R_{B1,i}^2)$ and $A_{w2} = \pi(R_{B2,o}^2 - R_{B2,i}^2)$.

The sorption rate into the adsorbent pellet was described by the following linear driving force (LDF) model with a single lumped mass transfer parameter, ω.[5,19]

$$\frac{\partial \overline{q_i}}{\partial t} = \omega_i \left(q_i^* - \overline{q_i}\right), \quad \omega_i = \frac{K D_{ei}}{r_c^2} \quad (9)$$

Table 3. LRC Parameters, LDF Coefficients, and Heat of Adsorption for Each Component

		Component			
	Unit	CO	CH_4	CO_2	H_2
ω_i	s^{-1}	0.0107	0.0585	0.0450	0.0200
$k_{1,i}$	10^{-3} mol/kg	0.0291	0.0229	0.0325	0.0187
$k_{2,i}$	10^{-8} mol/(kg K)	−6.0757	−5.8362	−9.1638	−1.4931
$k_{3,i}$	10^{-5} kPa^{-1}	9.22	4.2092	0.2578	0.0745
$k_{4,i}$	K	1012.8	1167.5	1191.2	1084.4
ΔH_i	J/mol	5240	4290	4300	2880

The multicomponent adsorption equilibrium was predicted by the following Loading Ratio Correlation (LRC) model:

$$q_i = \frac{q_{mi} B_i P_i}{1 + \sum_{j=1}^{n} B_j P_j} \tag{10}$$

where $q_m = k_1 + k_2 \times T$, $B = k_3 \exp(k_4/T)$.

The pressure drop across the bed was reflected by the following Ergun's equation[20–23]:

$$-\frac{dP}{dz} = a\,\mu u + b\,\rho u|u| \tag{11a}$$

$$a = \frac{150}{4R_p^2}\frac{(1-\varepsilon)^2}{\varepsilon^2}, \quad b = 1.75\,\frac{(1-\varepsilon)}{2R_p\varepsilon} \tag{11b}$$

where u is the interstitial velocity.

The boundary conditions of mass and energy balances for breakthrough run are presented later[8]:

$$-D_L\left(\frac{\partial c_i}{\partial z}\right)\bigg|_{z=0} = u\left(c_i|_{z=0^-} - c_i|_{z=0^+}\right); \quad \left(\frac{\partial c_i}{\partial z}\right)\bigg|_{z=L} = 0 \tag{12}$$

$$-K_L\left(\frac{\partial T}{\partial z}\right)\bigg|_{z=0} = \varepsilon\rho_g C_{pg} u\left(T|_{z=0^-} - T|_{z=0^+}\right); \quad \left(\frac{\partial T}{\partial z}\right)\bigg|_{z=L} = 0 \tag{13}$$

where $c_i|_{z=0^-}$ means feed concentration for component i.

In this study, before the breakthrough experiments, the separated experiments using N_2 at 323 K were performed to estimate the heat transfer coefficients in the bed packed with activated carbon. The heat transfer coefficients at the wall were determined by matching the energy balances in the bed and the wall to the experiment data.[24] However, because only two thermocouples could be installed in the inner bed, it was hard to obtain the accurate heat transfer coefficients from the separated experiments. Therefore, the obtained coefficients were used as the initial values to adjust the parameters to the adsorption and desorption experiments. And, the LRC parameters were obtained by using the isotherm results in the previous studies.[16,25] All the values using the mathematical model are listed in Tables 1 and 3.

Results and Discussion

Adsorption dynamics in single bed

The results of the breakthrough experiment and simulation in the single bed are shown in Figure 4. Hydrogen concentration drops first because of the early breakthrough of CO. Then, after decreasing smoothly with the breakthrough of CH_4, the H_2 concentration decreases rapidly because of the breakthrough of CO_2. The rolling-up phenomena of CO and CH_4 breakthrough curves were observed because of competitive adsorption with more strongly adsorbed component, CO_2. A small amount of CO_2 was detected at about 750 s, accompanying a significant temperature rise because of the strong adsorption affinity of CO_2. Therefore, the concentration and temperature wave fronts of CO_2 could have significant effects on the breakthrough curves of CO and CH_4. Because CO, the first breakthrough component, works as a critical impurity in the fuel cell application, it is needed to reduce the effects stemmed from CO_2 adsorption on CO adsorption.

Temperature profiles at 10 cm, 30 cm, 50 cm, and 75 cm from the feed end are presented in Figure 5. The experimental temperature histories agree well with the predicted results regardless of the location along the column length.

After steep temperature excursion, the temperature at each position decreased gently because of heat loss through the column wall. The temperature wave front shows a kind of inflection or plateau at which the roll-up phenomenon occurred. This can be explained by the fact that a competitive adsorption requires the heat of desorption for the less strongly adsorbed component in addition to the heat of adsorption for the more strongly adsorbed component. Therefore, the net heat generation would determine the extent of temperature rise.

Although, in this study, the experiments were conducted in a small-diameter column, the heat loss through the column wall was not sufficient for the system to be isothermal. Furthermore, the temperature excursion up to 32 K from the feed temperature and the tailing of the temperature profile have a detrimental influence on the adsorption dynamics

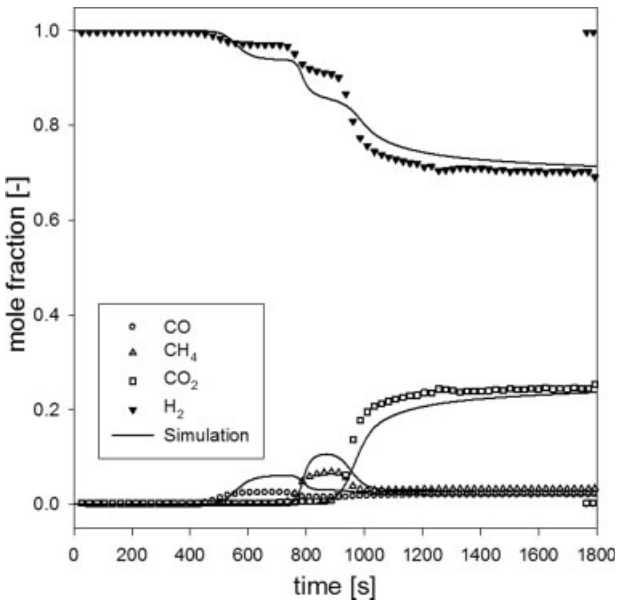

Figure 4. Experimental and simulated breakthrough curves in single bed under 7 LPM feed flow rate and 912 kPa adsorption pressure.

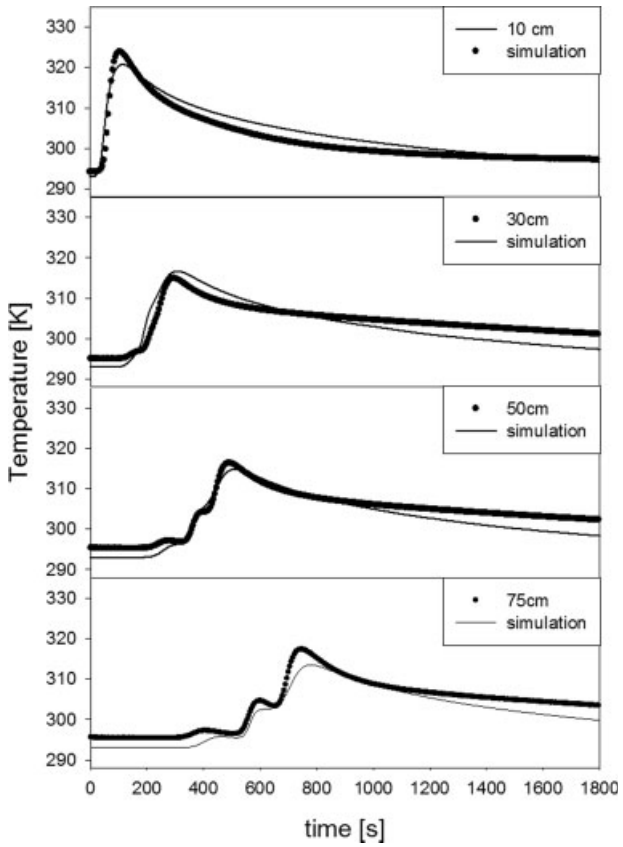

Figure 5. Temperature profile during single bed breakthrough experiment under 7 LPM feed flow rate and 912 kPa adsorption pressure.

because the adsorption isotherms of all the components on the activated carbon are significantly affected by a change in temperature.[26–28]

Adsorption dynamics in dual bed

Figure 6 shows the experimental and simulated breakthrough curves at the inner and outer beds, respectively. In this case, during the breakthrough experiment in one bed, no gas was supplied to the other bed. As shown in Figure 6(a), the breakthrough time and shape of each component in the inner bed are quite similar to the results for the single bed, even though the volume of the inner bed is smaller (81%) than that of the single bed. Furthermore, compared with the single and inner beds, the breakthrough times of CH_4 and CO_2 in the outer bed are prolonged as shown in Figure 6(b) although that of CO does not differ from the result for the inner bed. Also for the outer bed, the breakthrough curves of the impurities are sharper than those for the single and inner beds. The result implies that the shell-type bed leads to higher performance than the tube-type bed. Such improvement mainly stemmed from the heat exchange effect during adsorption. This can be proved by the inside temperature profiles of the inner and outer beds.

The heat of adsorption produced the temperature rise in the bed, in the same way as in the conventional bed. Temperature variations, with time at two locations of the inner bed and four locations of the outer bed, are presented in Figures 7 and 8.

As shown in Figure 7 for the inner bed breakthrough, the temperature excursion at the feed end of the inner bed (35 K) was slightly higher than that for the single bed in Figure 5, whereas the temperature excursion at the product end in each bed was quite similar. However, it is noteworthy that the temperature decrease in the inner bed is faster than that in the single bed after the temperature excursion. In addition, the small temperature increase was monitored in the outer bed as a result of heat exchange between the inner and outer beds. The heat exchange effect on the inner bed might contribute to the similar breakthrough performance to that of the single bed although the volume of the inner bed was small.

As shown in Figure 8 for the outer bed breakthrough, the temperature excursion in the outer bed was about 5 K during the breakthrough experiment. The temperature increase in the inner bed by heat transfer was interestingly similar to that in the outer bed. Since the shell-type outer bed has more than twice as much surface area for heat transfer than the inner bed, the thermal condition of the adsorption (outer) bed seemed to be near isothermal. Accordingly, the breakthrough

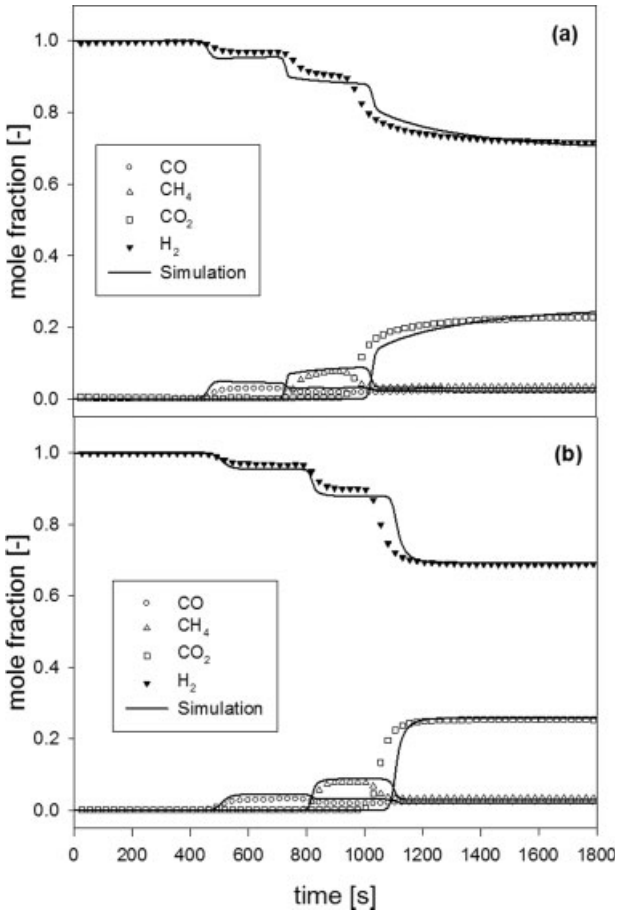

Figure 6. Experimental and simulated breakthrough curves in (a) inner bed and (b) outer bed under 7 LPM feed flow rate and 912 kPa adsorption pressure.

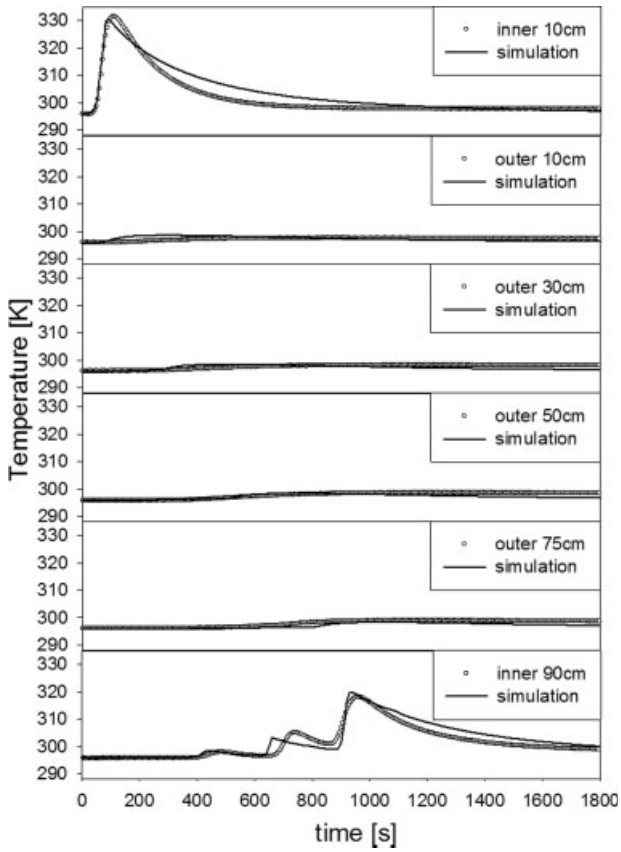

Figure 7. Temperature profile during inner bed breakthrough experiment under 7 LPM feed flow rate and 912 kPa adsorption pressure.

performance of the outer bed could show better performance than that of the single bed regardless of its smaller bed volume.

Breakthrough dynamics by simultaneous adsorption and desorption in dual bed

In the cyclic sequence of the two-bed PSA process (Figure 3), as the adsorption step is applied to one bed, the other bed works the desorption step. In this study, while one bed carried out adsorption breakthrough at the same condition to the previous breakthrough experiments (7 l per min (LPM) feed flow rate and 912 kPa adsorption pressure), the other bed performed simultaneously desorption breakthrough at 3.5LPM purge flow rate. The desorption experiment was performed using the bed, which was countercurrently depressurized after the adsorption breakthrough experiment.

Figures 9a and b show the adsorption breakthrough curves in the inner and outer beds, respectively, during desorption of the other corresponding bed. The breakthrough times of CO, CH_4, and CO_2 in each bed were longer than the results in Figure 6. Especially, note that the breakthrough time of CO was prolonged to more than 50 s at each bed compared with the result in the single bed, which could not be observed in the adsorption breakthrough without desorption. In addition, the roll-up of CO and CH_4 became smoother and less sharp than in previous results. Such improved adsorption capacity can contribute to the design of a more efficient PSA process.

As shown in Figure 10, the temperature profile at the feed end in the inner bed was almost the same as the result in Figure 7. However, at the end of bed, the temperature excursion was extended compared with Figure 7. Moreover, since the temperature observed was lower than feed until 500 s, the adsorption capacity could be improved, as shown in Figure 9(a). In addition, the outer bed seemed to act isothermally even though desorption is an endothermic process. As a result, it can be expected that the adsorption efficiency of the inner bed and the desorption efficiency of the outer bed are improved by the heat-exchange effect between these beds.

In the case of the adsorption breakthrough of the outer bed during the desorption breakthrough of the inner bed, the thermal dynamics observed differed from the previous case. As shown in Figure 11, the significant temperature decrease at both ends of the bed was observed for about 300–400 s, after which the temperature recovered to the feed temperature. On the other hand, the temperature in the outer bed during the adsorption breakthrough even decreased about 5 K, which was different from Figure 8. Therefore, this case also led to the performance improvement of the dual bed, as shown in Figure 9(b), compared to the single bed.

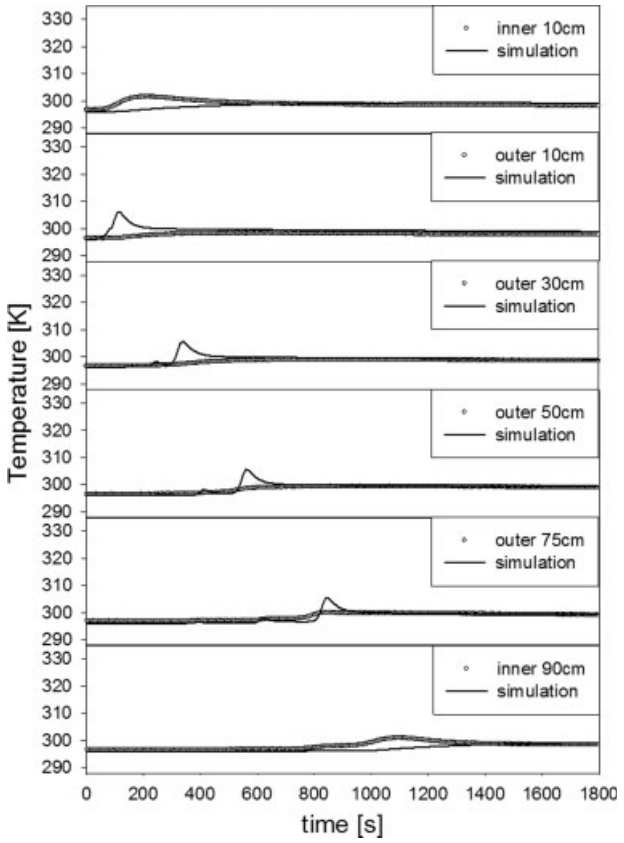

Figure 8. Temperature profile during outer bed breakthrough experiment under 7 LPM feed flow rate and 912 kPa adsorption pressure.

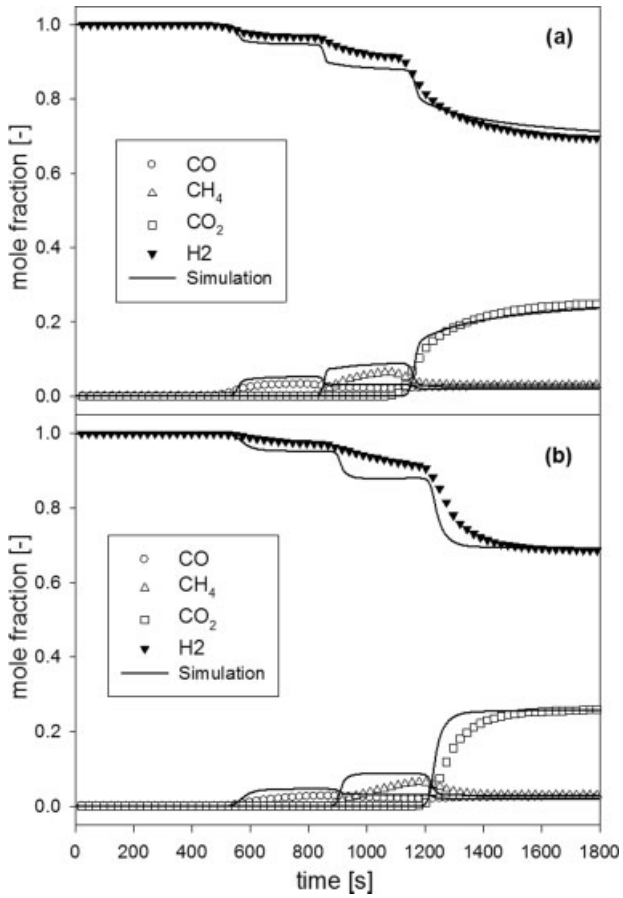

Figure 9. Experimental and simulated breakthrough curves (a) in inner bed with desorption in outer bed and (b) in outer bed with desorption in inner bed under 7 LPM feed flow rate, 912 kPa adsorption pressure, and 3.5LPM purge flow rate.

The predicted result for the concentration and temperature dynamics in the outer bed showed higher deviation from the experimental result than those in the inner bed as shown in Figures 9 and 11. The predicted result of the breakthrough curves in the outer bed was sharper than the experimental result. In addition, the small temperature excursion of the predicted result in the outer bed was not observed in the experimental result. It implies that the concentration and temperature profiles seem to be affected by the radial concentration and temperature gradients because the shell thickness of the outer bed is small. On the other hand, such phenomena were not observed in the inner bed which was covered by the outer bed. Therefore, the radial gradient effect will be reduced with an increase in the shell thickness of the outer bed as shown in the result of the inner bed.

Summarizing the above results, the thermal condition of the outer bed during operation becomes near isothermal because of the heat exchange effect between the beds as well as between the bed and its surroundings. On the other hand, the detrimental thermal effects in the inner bed can be reduced by the heat exchange between the beds. When the dual bed is applied to the PSA process, asymmetrical behavior will be observed which is not desirable. However, the dual bed can give the advantages of a compact PSA system as well as improved separation performance compared with a conventional PSA system.

Performance of the HE-PSA process

In this study, to produce high purity hydrogen from SMR, the HE-PSA using activated carbon was performed. The purge step by a weakly adsorbed component was primarily used to make a clean bed for the production of high-purity hydrogen. In this study, the purge-to-feed (P/F) ratio is defined as follows[5,19,29]:

$$\text{P/F ratio} = \frac{\text{Hydrogen used in PU step}}{\text{Hydrogen fed in AD step}}$$

The experimental results from the HE-PSA using one dual bed were compared with the simulated results for the conventional PSA using two single beds in Figures 12 and 13. Figure 12 shows the effect of adsorption (AD) step time on H_2 purity and recovery using the same feed flow rate, adsorption pressure, and purge rate. As expected from the

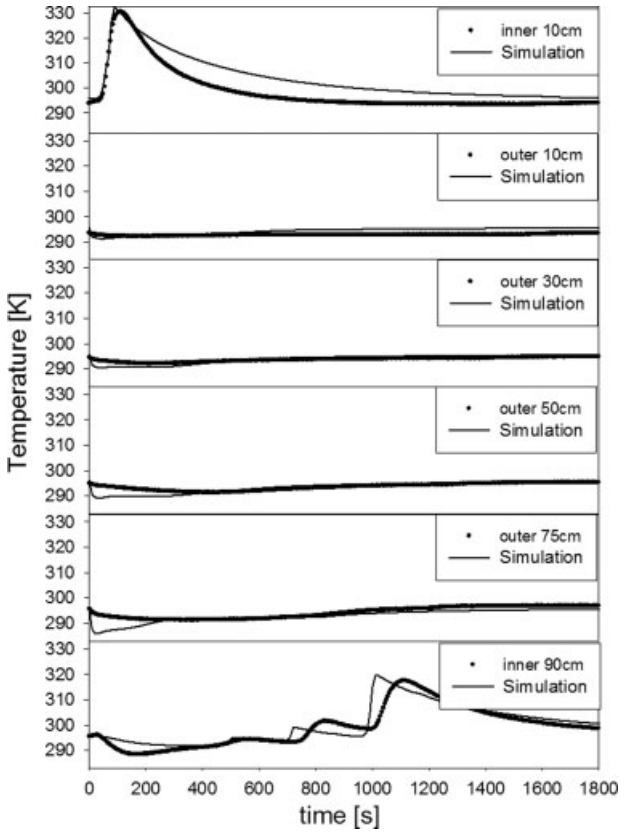

Figure 10. Temperature profile during adsorption in inner bed under 7 LPM feed flow rate and 912 kPa adsorption pressure and desorption in outer bed under 3.5 LPM purge flow rate.

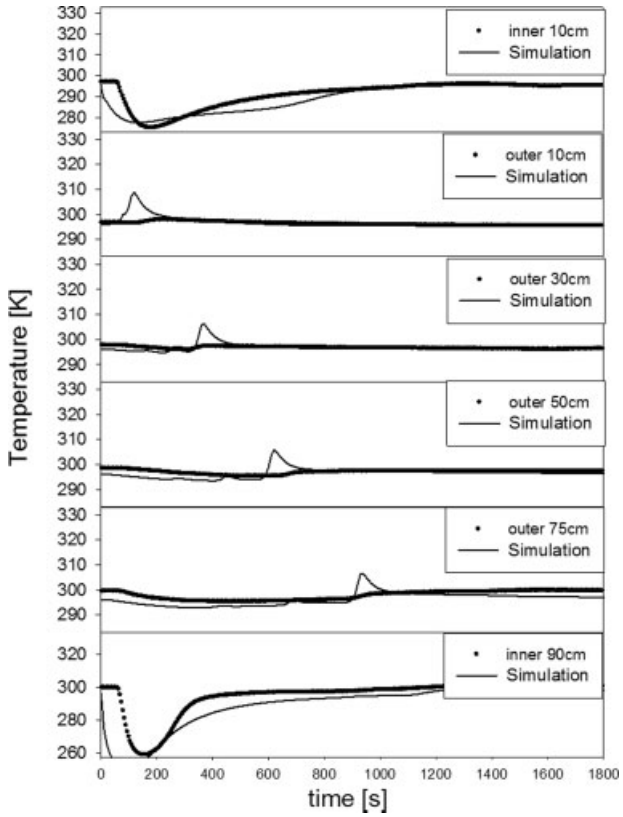

Figure 11. Temperature profile during adsorption in outer bed under 7 LPM feed flow rate and 912 kPa adsorption pressure and desorption in inner bed under 3.5 LPM purge flow rate.

breakthrough results, it was clearly presented that the performance of HE-PSA was higher than that of the conventional PSA although the HE-PSA used beds with a smaller volume than those for the single bed approach. Because of an increase in the AD step time, H_2 purity decreased marginally, but its recovery showed a slight increase. However, their variation in the experimental range was small compared with the results in the conventional PSA.

Figure 13 shows the effect of the purge rate on purity and recovery in the HE-PSA. When the P/F ratio increased, an increase in H_2 purity and a decrease in recovery were observed, following the typical performance of PSA processes. In addition, a sudden decrease to just below 98% in H_2 purity was observed when the purge rate was insufficient. Further, a difference in purity between the inner and outer bed was observed. On the basis of H_2 production higher than 99.9% in Figure 13, a P/F ratio of about 0.1 was likely to be the optimal value. The conventional PSA could almost attain the same level of purity with a significant sacrifice of recovery to the HE-PSA at ratio of 0.3 P/F. A further increase in the P/F ratio led to a decrease in H_2 recovery without a significant increase in purity. The difference in recovery between the HE-PSA and the conventional PSA was miniscule in the range of the applied P/F ratio, whereas the difference in purity was significant when the P/F ratio was low.

According to Figures 12 and 13, this implies that the performance of the HE-PSA was less affected by key operating variables such as AD step time and P/F ratio than that of the conventional PSA due to the heat exchange effect on the dual bed. Furthermore, it was clearly proved that the HE-PSA using the dual bed could produce high purity H_2 with a relatively small sacrifice of recovery compared with the conventional PSA. In addition, the HE-PSA could show higher separation performance by using a smaller amount of adsorbent than the conventional PSA.

However, the larger the diameter of the dual bed, the smaller the efficiency gains from heat exchange become because the temperature profiles of both inner and outer beds approach to the adiabatic behavior with an increase in the bed diameter. In such case, since the contact surface area is one of important factors in heat exchange, the contact surface area of the inner bed should be increased. One suggested method is that a bundle of inner tubes as an inner bed is applied to the dual bed so that the increased surface of a group of inner tubes leads to the improvement of heat transfer with an outer bed consisted of one shell tube. Therefore, the shape of the expected dual bed is similar to a shell-and-tubes heat exchanger whose volume of the shell is the same as that of the inner tubes.

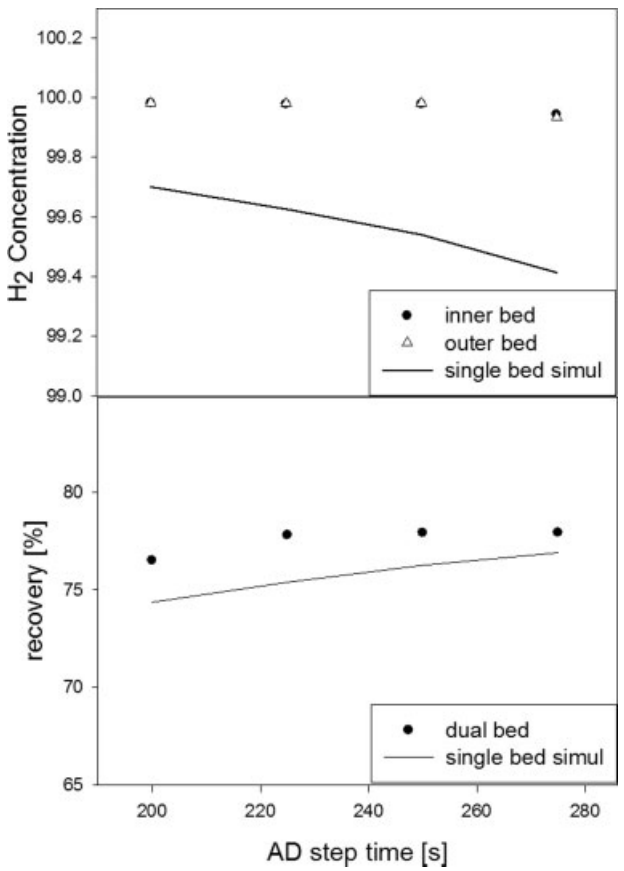

Figure 12. Effect of adsorption step time on H2 purity and recovery under 7 LPM feed flow rate, 912 kPa adsorption pressure, and 0.1 P/F ratio.

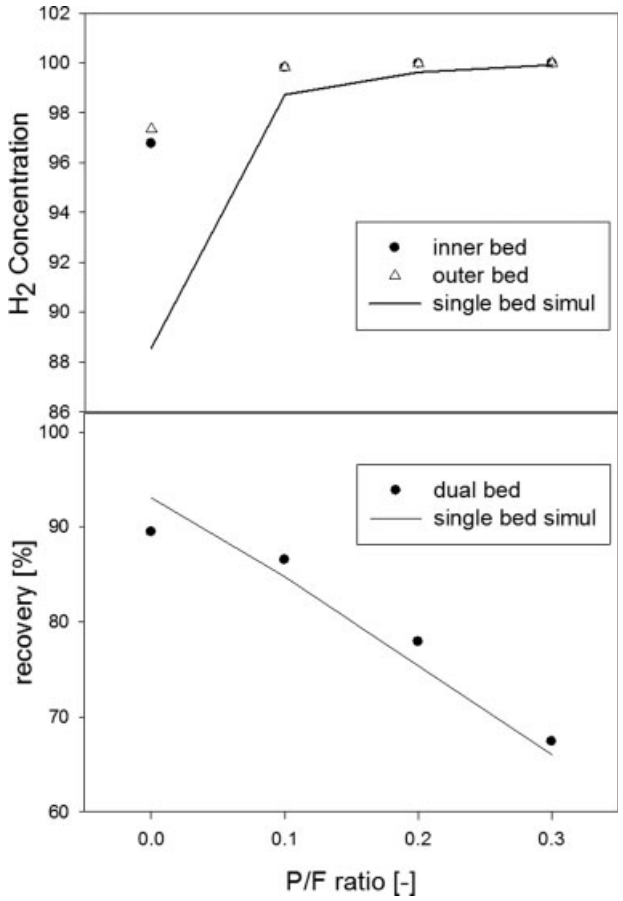

Figure 13. Effect of P/F ratio on H2 purity and recovery under 7 LPM feed flow rate, 912 kPa adsorption pressure, and 225 s AD step time.

Conclusions

The heat-exchange PSA (HE-PSA) was developed to design a compact PSA process as well as reduce the detrimental exothermic/endothermic heat effects accompanied by the adsorption/desorption steps. The dynamic behaviors of the annular-type dual used for the HE-PSA were studied.

Because of the heat exchange effects, the outer bed's activity mimicked isothermal behavior and the inner bed reduced the detrimental thermal effect on the bed's performance. As a result, the separation performance of the HE-PSA was higher than that of a conventional PSA at the same operating condition, even though a smaller amount of adsorbent was applied to the HE-PSA. In addition, compared with the conventional PSA, the high purity product could be obtained from the HE-PSA with a relatively small sacrifice of recovery.

Because the annular-type single bed acted as two beds in the HE-PSA process, the spatial occupancy of the beds and the amount of adsorbent could be significantly reduced, compared with a conventional PSA. Moreover, since the bed volume is proportionate to the radius square of the bed, the size increase of the dual bed would be insignificant in a real-world application, such as a hydrogen station. In addition, if the dual bed is designed on a large scale, using the concept of a shell-and-tubes heat exchanger, it is expected that the improved performance of the HE-PSA can be maintained due to the increased heat-exchange surface area of the inner and outer beds.

Acknowledgments

This work was supported by New & Renewable Energy R&D program (2004-N-HY12-P-01-0-000) under Ministry of Commerce, Industry and Energy (MOCIE) and SK Energy.

Notation

B = Langmuir-Freundlich isotherm parameter, kPa^{-1}
C_p = heat capacity, J/g K
D_L = mass axial dispersion coefficient, cm^2/s
h = heat transfer coefficient, J/cm s K
K = Proportionality parameter for the LDF model
K_L = effective axial thermal conductivity, J/cm s K
k = parameter for the Langmuir and LF model
n = Langmuir-Freundlich isotherm parameter
P = pressure, kPa
q_m = Langmuir-Freundlich isotherm parameter, mol/g
$\overline{q}$ = volume-averaged adsorbed phase concentration, mol/g
q^* = equilibrium adsorbed phase concentration, mol/g
Q = average isosteric heat of adsorption, J/mol or volumetric flow rate, cm^3/s ($=-\Delta H$)
R = radius, cm, or gas constant, J/mol · K
t = time, s
T = soild phase and gas phase temperature, K
T_{atm} = ambient temperature, K
u = interstitial velocity, cm/s
y = mole fraction in gas phase
z = axial position in a adsorption bed, cm

Greek letters

ε_t = total void fraction
ε = interparticle void fraction
μ = viscosity, cm/g s
v = superficial velocity, cm/s
ρ = density, cm^3/g
ω = LDF coefficient, s^{-1}

Subscripts

B = bed
c = crystal
i = component i, inner bed
o = outer bed
p = pellet
g = gas phase
s = solid phase
w = wall

Literature Cited

1. Balasubramanian B, Lopez OA, Kaytakoglu S, Harrison DP. Hydrogen from methane in a single-step process. *Chem Eng Sci*. 1999;54:3543–3552.
2. Abrardo JM, Khurana V. Hydrogen technologies to meet refiners' future needs. *Hydrocarbon Process*. 1995;79:43–49.
3. Rajesh JK, Gupta SK, Rangaiah GP, Ray AK. Multi-objective optimization of industrial hydrogen plants. *Chem Eng Sci*. 2001;56:999–1010.
4. Hufton JR, Mayorga S, Sircar S. Sorption-enhanced reaction process for hydrogen production. *AIChE J*. 1999;45:248–256.
5. Yang RT. *Gas Separation by Adsorption Processes*. Boston: Butterworths, 1987.

6. Suzuki M. *Adsorption Engineering*. Amsterdam: Elsevier, 1990.
7. Jee JG, Kim MB, Lee CH. Pressure swing adsorption processes to purify oxygen using a carbon molecular sieve. *Chem Eng Sci*. 2005;60:869–882.
8. Yang J, Chang JW, Lee CH. Separations of hydrogen mixtures by a two-bed pressure swing adsorption process using zeolite 5A. *Ind Eng Chem Res*. 1997;36:2789–2798.
9. Yang J, Han S, Cho C, Lee CH, Lee H. Bulk separation of hydrogen mixture by a one-column PSA process. *Sep Technol*. 1995;5:239–249.
10. Rota R, Wanket PC. Intensification of pressure swing adsorption processes. *AIChE J*. 1990;36:1299–1312.
11. Lee SJ, Hwan JJ, Moon JH, Jee JG, Lee CH. Parametric study of the three-bed PVSA process for high purity O_2 generation from ambient air. *Ind Eng Chem Res*. 2007;46:3720–3728.
12. Chou C, Huang WC. Simulation of a four-bed pressure swing adsorption process for oxygen enrichment. *Ind Eng Chem Res*. 1994;33:1250–1258.
13. Mendes AMM, Costa CAV, Rodrigues AE. Oxygen separation from air by PSA: modeling and experimental results part I: isothermal operation. *Sep Purif Technol*. 2001;24:173–188.
14. Farooq S, Ruthven DM. Dynamic of kinetically controlled binary adsorption in a fixed bed. *AIChE J*. 1991;37:299–301.
15. Ahn H, Chun C, Park M, Ahn IS, Lee CH. Thermal effects on the breakthrough curve of the hydrogen ternary system at a fixed bed. *Sep Sci Technol*. 2001;36:2121–2146.
16. Jee JG, Kim MB, Lee CH. Adsorption characteristics of hydrogen mixtures in a layered bed: binary, ternary, and five-component mixtures. *Ind Eng Chem Res*. 2001;40:868–878.
17. Doong SJ, Yang RT. Bulk separation of multicomponent gas mixtures by pressure swing adsorption: pore/surface diffusion and equilibrium models. *AIChE J*. 1986;32:397–410.
18. Malek A, Farooq S. Kinetics of hydrocarbon adsorption on activated carbon and silica gel. *AIChE J*. 1997;43:761–776.
19. Ruthven DM, Farooq S, Knaebel KS. *Pressure Swing Adsorption*. New York: VCH, 1994.
20. Sundaram N, Wankat PC. Pressure drop effects in the pressurization and blowdown steps of pressure swing adsorption. *Chem Eng Sci*. 1988;43:123–129.
21. Alpay E, Kenney CN, Scott DM. Simulation of rapid pressure swing adsorption and reaction processes. *Chem Eng Sci*. 1993;48:3173–3186.
22. Kikkinides ES, Yang RT. Effects of bed pressure drop on isothermal and adiabatic adsorber dynamics. *Chem Eng Sci*. 1993;48:1545–1555.
23. Lu ZP, Loureiro JM, Rodrigues AE, LeVan MD. Pressurization and blowdown of adsorption beds. II. Effect of the momentum and equilibrium relations on isothermal operation. *Chem Eng Sci*. 1993; 48:1699–1707.
24. Kim JH, Lee SJ, Kim MB, Lee JJ, Lee CH. Sorption equilibrium and thermal regeneration of acetone and toluene vapors on an activated carbon. *Ind Eng Chem Res*. 2007;46:4584–4594.
25. Yang J, Lee CH. Adsorption dynamics of a layered bed PSA for H_2 recovery from coke oven gas. *AIChE J*. 1998;44:1325–1334.
26. Bae YS, Lee CH. Sorption kinetics of eight gases on a carbon molecular sieve at elevated pressure. *Carbon*. 2004;43:95–107.
27. Kim MB, Bae YS, Choi DG, Lee CH. Kinetic separation of landfill gas by a two-bed pressure swing adsorption process packed with carbon molecular sieve: nonisothermal operation. *Ind Eng Chem Res*. 2006;45:5050–5058.
28. Kim MB, Bae YS, Ahn H, Lee CH. Comparison of adsorption dynamics in kinetic and equilibrium beds in hydrogen ternary system. *Sep Sci Technol*. 2004;39:2951–2976.
29. Jee JG, Lee SJ, Kim MB, Lee CH. Three-bed PVSA process for high purity oxygen from ambient air. *AIChE J*. 2005;51:2988–2999.

Manuscript received Oct. 23, 2007, and revision received Apr. 1, 2008.